Objective and structure of the thesis

Contents

1.1 Industrial context

The automotive industry has widely incorporated Advanced High Strength Steels sheets (AHSS) in vehicle structures due to their high strength to weight ratio: they are used to improve the vehicle safety or to reduce the vehicle weight through the use of thinner gages. At the same time, new vehicle design relies heavily on virtual prototyping practices. In the specific example of automotive structures, both the engineering of the production process and of the final product require reliable models of plasticity and fracture. Consequently, great efforts have been undertaken during the last five years to develop models that can predict the fracture of AHSS under static conditions (e.g. Wierzbicki et al., 2010, [190]). However, rates of deformation encountered in sheet metal forming operations are typically of the order of $10s^{-1}$, while they can be as high as $10^3\ s^{-1}$ under accidental crash loading. Therefore, there is a need to investigate the effect of strain rate on deformation behavior and fracture of AHSS, and to assess whether models developed for static loading conditions can satisfactorily be used in industrial applications.

Objective and structure of the thesis

This project was carried out in collaboration between the Solid Mechanics Laboratory (CNRS-UMR 7649, Ecole Polytechnique) and the Impact and Crashworthiness Laboratory (Massachusetts Institute of Technology).

The present research work consists of two main parts. The first part aims at developing a reliable methodology for evaluating the influence of strain rate as well as stress state on the ductile fracture properties of initially uncracked Advanced High Strength Steel sheets. An experimental procedure is designed to characterize the deformation behavior and the onset of fracture of sheet materials under tensile loading at high strain rate. Numerical and experimental validations of the proposed setup are performed to evaluate its accuracy. Then an experimental program is carried out at low, intermediate and high strain rates on different type of tensile specimens, thereby covering a range of stress states. Detailed Finite Element analyses of each experiment are used to determine the loading history and the material state at fracture in each experiment. A key component of this hybrid experimental-numerical approach is the constitutive model: a rate-dependent plasticity model is proposed to predict the mechanical response of AHSS over all the range of strains, strain rates and stress states reached in the experiments. The model accuracy is validated by comparing global and local test measurements to the corresponding simulation predictions. In addition, the influence of the geometric discretization used in Finite Element analysis on the accuracy of the hybrid experimental-numerical approach is evaluated. It is shown that fine meshes of brick elements are required for accurate fracture predictions, but cannot be used in industrial applications because of inadequate computational efficiency. A technique of shell-to-solid re-meshing is presented and evaluated, that allows for accurate predictions of the onset of ductile fracture in sheet materials without compromising the numerical efficiency of shell elements.

The second part of this work is concerned with the micro-mechanisms responsible for ductile failure. Micrographs of specimens corresponding to different stages of loading prior to failure are analyzed to identify the sequence of damage processes leading to fracture. Observations suggest that the governing failure mechanism is the localization of plastic deformation into shear bands at the grain level.

A numerical model based on three dimensional unit cell calculations is developed to assess whether the mechanism of shear localization of the plastic flow at the micro-scale can explain the dependence of the material ductility to both stress state and strain rate that was observed at the macro-scale.

The thesis is organized as follow:

In Chapter 2, background information is given on the characterization and modeling of plasticity and ductile fracture of AHSS under static loading conditions. In addition, variables that will be used throughout the manuscript to describe the stress state are precisely defined. Finally, Split Hopkinson Pressure Bar systems, used for characterizing mechanical behavior of materials under compression at high rates of deformation, are presented.

In Chapter 3, a high strain rate tensile testing technique for sheet materials is presented which makes use of a modified split Hopkinson pressure bar system in conjunction with a load inversion device. With compressive loads applied to its boundaries, the load inversion device introduces tension into a sheet specimen. Detailed finite element analysis of the experimental set-up is performed to validate the design of the load inversion device. It is shown that under the assumption of perfect alignment and slip-free attachment of the specimen, the measured stress-strain curve is free from spurious oscillations at a strain rate of $1000s^{-1}$. Validation experiments are carried out using tensile specimens, confirming the oscillation-free numerical results in an approximate manner.

In Chapter 4, the effect of strain rate on ductile fracture properties of the TRIP material is characterized using a hybrid experimental-numerical method. Tensile experiments are carried out at low ($\dot{\varepsilon}\sim 10^{-3}s^{-1}$), intermediate ($\dot{\varepsilon}\sim 1s^{-1}$) and high strain rates ($\dot{\varepsilon}\sim 10^{3}s^{-1}$). The experimental program includes notched as well as uniaxial tension specimens. Local displacements and surface strain fields are measured optically in all experiments using Digital Image Correlation. Constitutive equations derived from the Mechanical Threshold Stress theory are proposed to describe the rate-dependent behavior as well as plastic anisotropy of the sheet material. Detailed Finite Element simulations of all experiments reveal that the model accurately predicts experimental results, including force displacement curves and local surface strain evolution. In particular, the behavior at large strain (beyond the onset of necking) is well predicted. Stress and strain histories where fracture initiates are also obtained from the simulations in order to characterize the dependence of the material ductility to both strain rate and stress state. If the fracture strain is higher at high strain rate in all experiments, results show that the effect of strain rate on ductility cannot be considered independently from the state of stress.

In Chapter 5, the influence of the finite element modeling on predictions of mechanical response and ductile fracture in sheet structures is analysed. The inability of shell elements to accurately predict the post-necking behavior of sheet materials is highligted. On the contrary predictions independent from the mesh characteristics are obtained with solid elements if sufficiently fine meshes are used. However, intensive computation efforts associated with the use of fine meshes of solid elements to model sheet structures such as automotive parts make it unsuitable to an industrial environment. A dynamic shell-to-solid re-meshing technique is considered to benefit from both the numerical efficiency of shells and the accuracy of fine solid meshes. Comparisons between numercial predictions using re-meshing and experimental results show a significant increase of the accuracy of fracture predictions compared to shell simulations, and substantial time savings compared to solid simulations.

In Chapter 6, the evolution of damage and the mechanisms responsible for ductile failure are identified in the TRIP steel sheet submitted to different stress states, using optical and scanning electron microscopy. Experiments are performed on tensile specimens and on disk specimens submitted to out-of-plane hemispherical punching, thereby covering stress states from uniaxial to equi-biaxial tension. For each specimen geometry, experiments have been interrupted prior to fracture at different stages of deformation: onset of through the thickness necking and 95%, 99% of the displacement at which fracture initiates. Micrographs of samples extracted from the deformed specimens permit to evaluate the material damage for increasing amounts of accumulated plastic strain, and identify rupture mechanisms. It is shown that the critical mechanism responsible for material failure is the localization of the plastic deformation in a shear band initiating at a grown and isolated void. The orientation of the fracture surface is controlled by the shear band direction.

In Chapter 7, a numerical model is developped to investigate the influence of the stress state and strain rate on the onset of localization of the plastic flow in a void-containing material. A three-dimensional unit cell containing an initially spherical void is submitted to proportional loadings in the macroscopic stress space. Fully periodic boundary conditions are applied. The range of stress states considered are limited to biaxial tension, i.e. from uniaxial to equi-biaxial tension under plane stress conditions. The model is able to predict qualitatively the dependence of ductility to the stress state observed experimentaly, as well as the increase of ductility at high strain rate.

1.3 Material

All the experimental work presented in this manuscript is performed on specimens extracted from 1.4mm thick TRIP780 steel sheets provided by POSCO (Korea). This particular representative of the AHSS family has been chosen as its plastic behavior and ductile fracture properties under static loading conditions have been extensively studied (Mohr et al., 2010, [122]; Dunand and Mohr, 2010, 2011, [48-50]). The chemical composition of the present TRIP780 material as measured by energy-dispersive X-ray analysis is given in Table 1-1. Micrographs (Fig. 1-1) reveal a fine grain structure with a maximum grain size of about $10\mu m$ and show that martensite and austenite grains (in blue/brown in Fig. 1-1) tend to segregate in bands parallel to the sheet rolling direction.

Table 1-1: Chemical composition of the TRIP780 material in wt-%

C	Al	Mn	Si	Mo
1.70	0.47	2.50	0.59	0.08

TRansformation Induced Plasticity (TRIP) steels present complex multi-phase microstructures consisting of a ferritic matrix and a dispersion of multiphase grains of bainite, martensite and metastable retained austenite (Jacques et al., 2001, [86]). The austenitic phase transforms to martensite when subject to mechanical or thermal loading (e.g. Angel, 1954, [4]; Lecroisey and Pineau, 1972, [103]; Olsen and Cohen, 1975, [142]; Stringfellow et al.,1992, [167]). The austenite-to-martensite formation is displacive which gives rise to internal stresses that may cause the yielding of the surrounding austenite matrix (e.g. Greenwood and Johnson, 1965, [69]). The active formation of martensite substantially increases the macroscopic work-hardening rate while the associated transformation strain contributes to the ductility of TRIP steels.

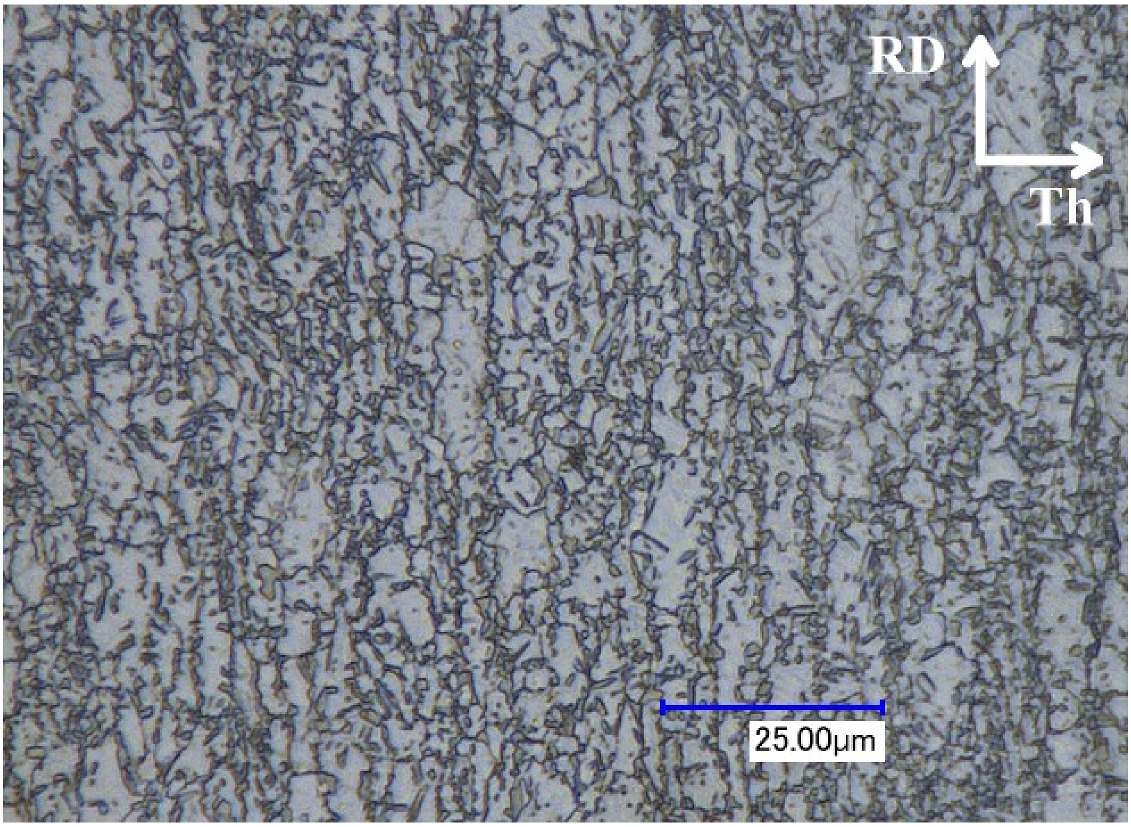

Figure 1-1: Optical micrograph of the undeformed TRIP material. The *RD* and *Th* orientations correspond to the sheet rolling and through-the-thickness directions, respectively.

Chapter 2

Preliminaries

Contents

Abstract

Variables that will be used throughout the manuscript to describe the stress state are precisely defined. In addition, background information is given on the characterization and modeling of plasticity and ductile fracture of AHSS under static loading conditions. Finally, Split Hopkinson Pressure Bar systems, used for characterizing mechanical behavior of materials under compression at high rates of deformation, are presented.

2.1 Characterization of the stress state

2.1.1 Stress invariants

Throughout our discussion, a clear description of the stress state is important. The frame invariant part of the stress is described through the first invariant of the Cauchy stress tensor $\boldsymbol{\sigma}$, and the second and third invariants of the corresponding deviatoric stress tensor, $\boldsymbol{s} = \boldsymbol{\sigma} - (\mathrm{tr}\boldsymbol{\sigma}/3)\mathbf{1}$,

$$I_1 = \mathrm{tr}(\boldsymbol{\sigma}) \tag{2-1}$$

$$J_2 = \frac{1}{2}\boldsymbol{s}:\boldsymbol{s} \tag{2-2}$$

and

$$J_3 = \det(\boldsymbol{s}) \tag{2-3}$$

Note that the hydrostatic stress σ_m and the von Mises equivalent stress σ_{VM} are respectively proportional to the first and second invariants,

$$\sigma_m = \frac{1}{3}I_1 \tag{2-4}$$

$$\sigma_{VM} = \sqrt{3J_2} \tag{2-5}$$

The stress state may be characterized through two dimensionless functions of the above invariants. We define the stress triaxiality η as the ratio of the mean stress and equivalent von Mises stress,

$$\eta = \frac{\sigma_m}{\sigma_{VM}} = \frac{\mathrm{I}_1}{3\sqrt{3J_2}} \tag{2-6}$$

with $-\infty \leq \eta \leq \infty$. The normalized third invariant ξ_3 is written as (Ilyushin, 1963, [84])

$$\xi_3 = \frac{27}{2}\frac{J_3}{{\sigma_{VM}}^3} = \frac{3\sqrt{3}}{2}\frac{J_3}{{J_2}^{\frac{3}{2}}} \tag{2-7}$$

and lies in the range $-1 \leq \xi_3 \leq 1$; it characterizes the position of the second principal stress σ_{II} with respect to the maximum and minimum principal stresses σ_I and σ_{III}.

Alternatively the third invariant can be described in terms of the so-called Lode angle parameter

$$\bar{\theta} = 1 - \frac{2}{\pi}\arccos(\xi_3) \tag{2-8}$$

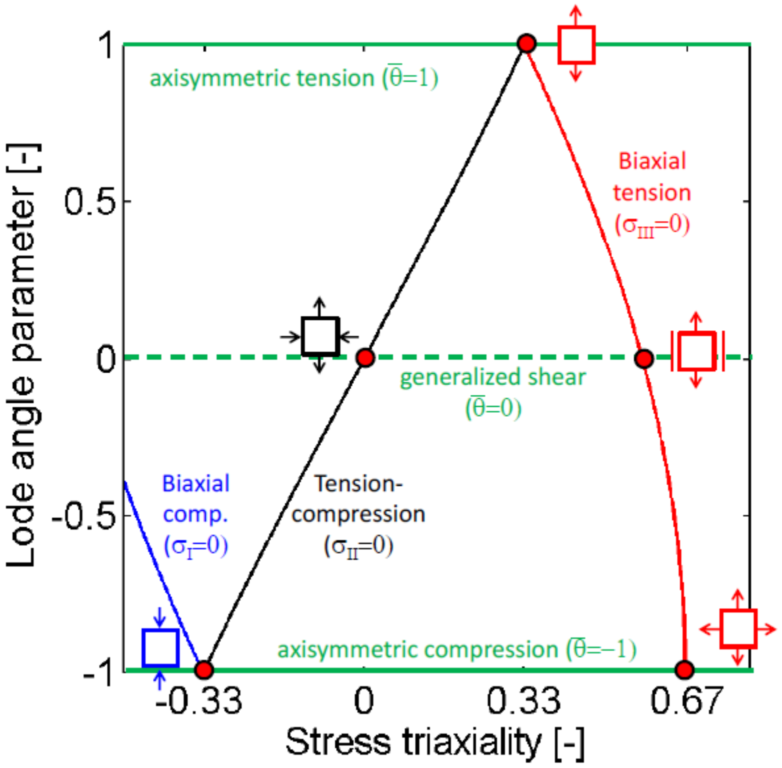

Figure 2-1: Characterization of the stress states in terms of stress triaxiality and Lode angle parameter. The blue, black and red lines highlight the plane stress states as described by Eq. (2-16).

According to the definition above, the Lode angle parameter approximates the negative Lode number μ (Lode, 1925, [113]),

$$\mu = 2\frac{\sigma_{II} - \sigma_{III}}{\sigma_I - \sigma_{III}} - 1 \cong -\bar{\theta} \tag{2-9}$$

Note that the principal stresses σ_I, σ_{II} and σ_{III} are got back using

$$\sigma_I = \bar{\sigma}[\eta + f_I(\bar{\theta})] \tag{2-10}$$

$$\sigma_{II} = \bar{\sigma}[\eta + f_{II}(\bar{\theta})] \tag{2-11}$$

$$\sigma_{III} = \bar{\sigma}[\eta + f_{III}(\bar{\theta})] \tag{2-12}$$

with the deviator dependent functions

$$f_I(\bar{\theta}) = \frac{2}{3}\cos\left(\frac{\pi}{6}(1-\bar{\theta})\right) \tag{2-13}$$

$$f_{II}(\bar{\theta}) = \frac{2}{3}\cos\left(\frac{\pi}{6}(3+\bar{\theta})\right) \tag{2-14}$$

$$f_{III}(\bar{\theta}) = -\frac{2}{3}\cos\left(\frac{\pi}{6}(1+\bar{\theta})\right) \tag{2-15}$$

Throughout this manuscript, the term stress state is employed to make reference to the pair of parameters $(\eta, \bar{\theta})$. Well-known stress states that we will refer to frequently are:

- Uniaxial tension ($\eta = 0.33, \bar{\theta} = 1$)
- Pure shear ($\eta = 0., \bar{\theta} = 0$)
- Generalized shear ($\bar{\theta} = 0$)
- Axisymmetric tension ($\bar{\theta} = 1$)
- Axisymmetric compression ($\bar{\theta} = -1$)

A representation of the $(\eta, \bar{\theta})$ stress state space is depicted in Fig. 2-1.

2.1.2 Plane stress condition

In sheet materials, the plane stress condition often prevails: one of the principal stress directions is parallel to the sheet thickness direction and the corresponding principal stress is equal to zero.

In case of plane stress, the stress triaxiality η and the normalized third invariant ξ are uniquely related according to the relationship

$$\xi_3 = -\frac{27}{2}\eta\left(\eta^2 - \frac{1}{3}\right) \quad \text{for} \quad -\frac{2}{3} \leq \eta \leq \frac{2}{3} \tag{2-16}$$

In this investigation we focus more specifically on stress states in the vicinity of biaxial tension, i.e. plane stress states between uniaxial tension and equi-biaxial tension. In this case the stress triaxiality varies between 1/3 (uniaxial tension) and 2/3 (equi-biaxial

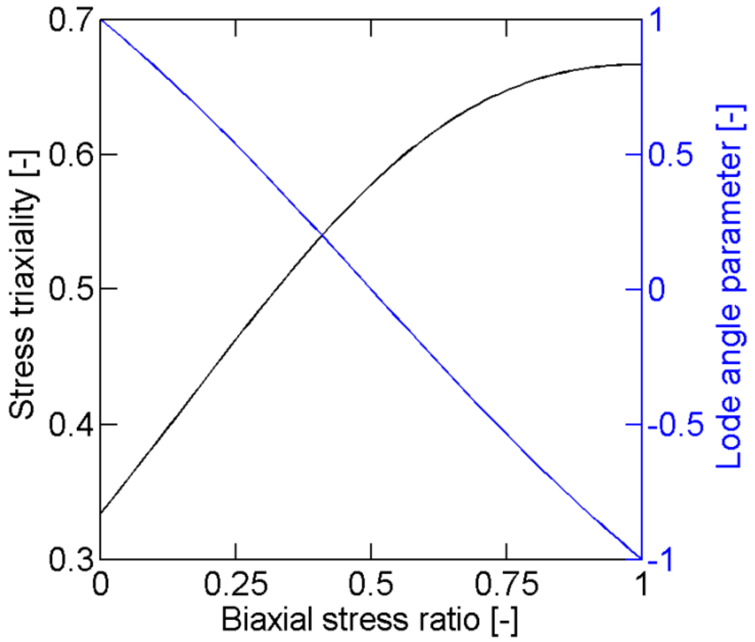

Figure 2-2: Relation between the stress triaxiality η, the Lode angle parameter $\bar{\theta}$ and the stress ratio ψ in case of biaxial stress states.

tension). At the same time, the third invariant decreases from 1 (uniaxial tension) to -1 (equi-biaxial tension).

Denoting $\sigma_I \geq \sigma_{II} \geq \sigma_{III}$, $\sigma_{III} = 0$ the principal values of the Cauchy stress tensor, the stress state in biaxial tension is then fully characterized by the biaxial stress ratio

$$\psi = \frac{\sigma_{II}}{\sigma_I} \tag{2-17}$$

with $0 \leq \psi \leq 1$. The stress triaxiality then reads

$$\eta = \frac{1+\psi}{3\sqrt{\psi^2 - \psi + 1}} \tag{2-18}$$

Figure 2-2 depicts the relationship between the stress triaxiality η (black line in Fig. 2-2) and the Lode angle parameter $\bar{\theta}$ (blue line in Fig. 2-2) to the biaxial stress ratio in case of a biaxial stress state.

2.2 Ductile fracture modeling

Ductile fracture is the result of a progressive material deterioration occurring during plastic deformation, generally identified as the nucleation and growth of micro-voids that ultimately link to form cracks. The early investigations of McClintock (1968, [119]) and Rice and Tracey (1969, [152]) on the evolution of cylindrical and spherical holes in ductile matrices have set the foundation for numerous studies on the micromechanics associated with void growth. The most prominent is that of Gurson (1977, [70]), who proposed a porous plasticity model based on the micromechanical analysis of a thick spherical shell subject to hydrostatic pressure. The model describes the growth of voids and its influence on the material's stress carrying capacity at large mean stresses (but becomes less accurate for shear loads). The original Gurson model has been repeatedly modified to account for additional processes responsible for the material deterioration and subsequent ductile fracture: void nucleation (e.g. Chu and Needleman, 1980, [35]), loss of load-carrying capacity associated with void coalescence (e.g. Tvergaard and Needleman, 1984, [181]), enhanced strain hardening models (e.g. Leblond et al., 1995, [102]), void shape effects (e.g. Gologanu et al., 1993, [67]; Gologanu et al., 1994, [68]; Garajeu et al., 2000, [62]; Pardoen and Hutchinson, 2000, [146]) and plastic anisotropy (e.g. Benzerga et al., 2004, [18]). The reader is referred to Lassance et al. (2007, [100]) and Benzerga and Leblond (2010, [19]) for a comprehensive review of successive improvements of the Gurson model. Gurson type of models are not only used to describe macroscopic plastic behavior of materials with small void volume fractions, but also to predict ductile fracture assuming that fracture occurs as the void volume fraction reaches a critical value. As a result, "traditional" Gurson models are unable to predict fracture under shear-dominated loading conditions, where the void growth mechanism is inactive. Numerical investigations of an initially spherical void contained in a cubic unit cell submitted to various tri-axial loadings (e.g. Zhang et al., 2001, [196]; Gao and Kim, 2006, [59]) showed that the third stress invariant (or Lode parameter) has a strong influence on void shape evolution and on coalescence. The influence of the third stress invariant on the ductility of metals is

---

[1] This Section is reproduced from: Dunand, M. and D. Mohr (2011). "On the predictive capabilities of the shear modified Gurson and the modified Mohr–Coulomb fracture models over a wide range of stress triaxialities and Lode angles". *Journal of the Mechanics and Physics of Solids* **59**(7): p. 1374-1394.

also shown experimentally (e.g. Barsoum and Faleskog, 2007, [15]). This particular shortcoming of Gurson models has been addressed by the recent models of Xue (2008, [193]) and Nahshon and Hutchinson (2008, [130]). The latter consider the void volume fraction as damage parameter, and introduce a dependency of the damage evolution on the third stress invariant. This empirical modification has been introduced in an ad-hoc manner to deal with the material deterioration due to void distortion and inter-void linking under shearing. As a result, the Nahshon-Hutchinson model can predict failure under shear-dominated loading, such as during the cutting of sheet metal (Nahshon and Xue, 2009, [131]). However, Nielsen and Tvergaard (2009, [137]) found that this modification is inadequate in the case of high stress triaxialities, compromising the predictive capabilities of the original Gurson model for loading conditions where void growth is the main damage mechanism. Consequently, Nielsen and Tvergaard (2010, [138]) proposed a slight modification of the Nahshon-Hutchinson model, making the damage accumulation under shear-dominated stress states active only for low stress triaxialities. It is noted that these two recent shear-modified Gurson models do not account for the effect of void distortion at large shear strains. Micromechanical models that are able to deal with general ellipsoidal void shape evolution are still at an early stage of development and require further validation (e.g. Leblond-Gologanu, 2008, [101]).

As an alternative to Gurson type of models, uncoupled fracture models have been developed for metals where standard incompressible plasticity models are used in conjunction with a separate fracture model (e.g. Fischer et al., 1995, [57]). Unlike in Gurson models, it is assumed that the evolution of damage has no effect on the effective stress-strain response of the material before fracture occurs. Within this framework, damage is measured through the scalar variable $D,$ and its increase $dD \geq 0$ is defined though the increment of the equivalent plastic strain $\bar{\varepsilon}^p$ with respect to a stress-state dependent reference failure strain $\hat{\epsilon}$,

$$\mathrm{dD} = \frac{d\bar{\varepsilon}^p}{\hat{\varepsilon}(\boldsymbol{\sigma})} \tag{2-19}$$

Assuming an initial value of $D = 0$ for the material in its undeformed configuration, it is postulated that fracture initiates as $D = 1$. The reference failure strain may be interpreted as a weighting function and corresponds to the strain to fracture for monotonic proportional loading. It is either chosen empirically or inspired by micromechanical results. A comparative study of various weighting functions (including models based on the work of McClintock (1968, [119]), Rice and Tracey (1969, [152]), LeRoy et al. (1981, [108]), Cockcroft and Latham (1968, [37]), Oh et al. (1979, [140]), Brozzo et al. (1972, [24]), and Clift et al. (1990, [36])) showed that none of them can accurately describe the fracture behavior of a aluminum 2024 over a large range of stress triaxialities (Bao and Wierzbicki, 2004, [11]). Wilkins et al. (1980, [192]) proposed a weighting function depending on the asymmetry of the deviatoric principal stresses in addition to hydrostatic pressure. It was assumed that the effect of hydrostatic pressure and stress asymmetry on ductility were separable. Attempts to define a more general fracture criterion have lead to the introduction of the third invariant of the stress tensor in the weighting function (e.g. Wierzbicki and Xue, 2005, [191]). Recently, Bai and Wierzbicki (2010, [6]) transposed the classical Mohr Coulomb fracture criterion into the space of stress triaxiality, Lode angle and equivalent plastic strain, defining the so-called Modified Mohr-Coulomb (MMC) fracture criterion.

There exist two more widely-used alternatives to the above two modeling approaches: Continuum Damage Mechanics (CDM) and Forming Limit Curves (FLC). In the framework of Continuum Damage Mechanics, material degradation is modeled through an internal damage variable while the constitutive equations are derived from the first and second principles of thermodynamics for continuous media (e.g. Lemaitre, 1985, [107]; Chaboche, 1988, [31, 32]). Most sheet metal forming processes are still designed against failure based on the concept of FLCs. The FLC is typically constructed in the space of the principal in-plane strains based on the experimental results for uniaxial tension and a series of Nakazima tests (e.g. Banabic et al., 2000, [9]). It is then assumed that failure (either necking or fracture) occurs as the strain path in a sheet metal forming operation crosses the FLC. In this approach, it is assumed that the FLC is independent of the loading path.

2.3 Rate-independent plasticity of AHSS

From a mechanical point of view, TRIP-assisted steels may be considered as composite materials at the micro-scale. Papatriantafillou et al. (2006, [145]) made use of homogenization techniques for nonlinear composites (e.g. Ponte Castaneda, 1992, [148]) to estimate the effective properties of TRIP-assisted steels. Based on the work by Stringfellow et al. (1992, [167]) for fully austenitic TRIP steels, Papatriantafillou et al. (2006, [145]) formulated the computational procedure for a four phase metallic composite with evolving phase volume fractions and isotropic viscoplastic phase behavior. Turteltaub and Suiker (2005, [176]) presented a more detailed multi-scale model for TRIP-assisted steels which includes anisotropic features associated with the phase crystal orientations and the martensite twinning. A mean-field model which describes DP steels as a composite of isotropic elasto-plastic phases with spherical inclusions has been proposed by Delannay et al. (2007, [44]). This model has been enhanced further to TRIP-assisted steels (Delannay et al., 2008, [45]) using the assumption that spherical austenite inclusions transform instantaneously into spherical martensite inclusions. Based on the intermediate strain rate tensile testing of TRIP600 and DP600 steels, Huh et al. (2008, [82]) conclude that both the flow and ultimate tensile strength increase as the level of pre-strain increases.

Most AHSS exhibit a pronounced Bauschinger effect. Banu et al. (2006, [10]) adopted an isotropic Swift law combined with saturated kinematic hardening of the Amstrong-Frederick type to model a series of Bauschinger simple shear tests on a DP600 steel. The accurate modeling of the cyclic behavior of AHSS is important in drawing operations where the sheet material is both bent and unbent. Using a stack of laminated dogbone specimens along with an anti-buckling device, Yoshida et al. (2002, [194]) measured the response of a DP590 steel under cyclic uniaxial tension-compression loading at large strains. Their study shows that the combination of isotropic, non-linear kinematic and linear kinematic hardening provides a satisfactory model for the observed transient and permanent softening in the dual phase steel. As Yoshida et al. (2002, [194]), Lee et al. (2005, [105]) emphasize the importance of an

---

[2] This Section is reproduced from: Mohr, D., M. Dunand, and K.H. Kim (2010). "Evaluation of associated and non-associated quadratic plasticity models for advanced high strength steel sheets under multi-axial loading". *International Journal of Plasticity* **26**(7): p. 939-956.

accurate description of the Bauschinger and transient behavior in view of springback computations. Based on the comparison of uniaxial experiments on a DP steel and simulations, Lee et al. (2005, [105]) concluded that a modified Chaboche type combined isotropic-kinematic hardening law provides a good representation of the Bauschinger and transient behavior. However, a recent study by Tarigopula et al. (2008, [172]) on a DP800 steel demonstrated that the modeling of transient anisotropy in plastic flow induced by strain-path changes cannot be represented correctly when using a non-linear combined isotropic-kinematic hardening model. Broggiato et al. (2008, [22]) performed 3-point-bending tests on two DP600 and a TRIP700 steel. Their results show that the cyclic hardening behavior of both steel grades is very similar and can be modeled using a non-linear combined isotropic-kinematic hardening model. Using a double-wedge device, Cao et al. (2008, [29]) performed uni-axial tension-compression tests on 1.6mm thick DP600 steel. They modeled their experiments using using a modified Chaboche type combined isotropic-kinematic hardening law (with permanent softening and non-symmetric reloading) as well as the two-surface model by Lee et al. (2007, [104]). Note that the present thesis focuses only on monotonic loadings of the sheet material. Considerations on possible kinematic hardening will therefore be disregarded in the present work.

Different yield surfaces have been used in the past to model advanced high strength steels: von Mises yield surface (e.g. Yoshida et al., 2002, [194]; Durrenberger et al., 2007, [51]), quadratic anisotropic Hill (1948, [78]) yield function (e.g. Banu et al., 2006, [10]; Padmanabhan et al., 2007, [143]; Broggiato et al., 2008, [22]; Chen and Koc, 2007, [34]), high exponent isotropic Hershey (1954, [77]) yield function (Tarigopula et al., 2008, [172]), non-quadratic anisotropic Barlat (2003, [13]) yield function (Lee et al., 2005, 2008, [105, 106]). The reader is referred to Chaboche (2008, [33]) for a recent review of macroscopic plasticity theories.

The plastic behavior of the present TRIP780 material has been extensively characterized by Mohr et al. (2010, [122]). Using both uniaxial tension as well as biaxial shear-tension experiments (Mohr & Oswald, 2008, [126]), they measured the material response at low strain rate for more than twenty different stress states in the range of pure shear to transverse plane strain tension. A characteristic feature of this material is that almost same stress-strain curves are measured for uniaxial tension along different material orientations (as shown in Fig. 2-3), indicating a planar isotropic yield behavior. At the same time the plastic flow exhibits a strong anisotropy: the Lankford ratios[3] are r_0=0.67, r_{45}=0.96 and r_{90}=0.85 for tension along the rolling direction, the 45° direction and the transverse direction, respectively. Mohr et al. (2010, [122]) proposed a rate-independent plasticity model made of (a) a planar isotropic quadratic yield surface, (b) a orthotropic quadratic non-associated flow rule and (c) isotropic strain hardening to capture this behavior.

Note that the discussion of non-associated formulations in metal plasticity has been partially initiated by the experimental observations of Spitzig and Richmond (1984, [162]). Non-associated plasticity models for metals have been considered by Casey and Sullivan (1985, [30]), Brünig and Obrecht (1998, [27]), Brünig (1999, [25]), Lademo et al. (1999, [99]), Stoughton (2002, [164]), Stoughton and Yoon (2004, 2008, [165, 166]) and Cvitanic et al. (2008, [41]).

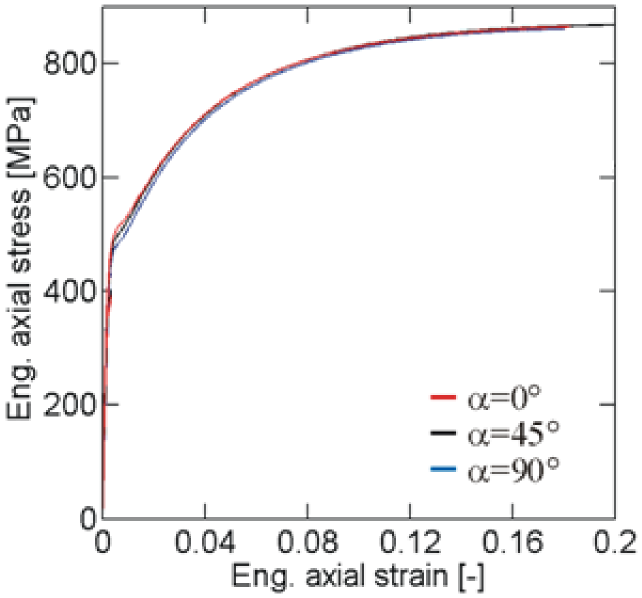

Figure 2-3: Uniaxial tensile testing – engineering stress strain curve along the sheet rolling direction (red), transverse direction (blue) and 45° direction (black).

---

[3] Lankford ratios, or r-values, characterize the preferred direction of plastic flow under uniaxial tension and correspond to the ratio of width to thickness plastic strain rate: $r = d\varepsilon_w^p / d\varepsilon_{th}^p$. They are a widely used indicator of plastic anisotropy.

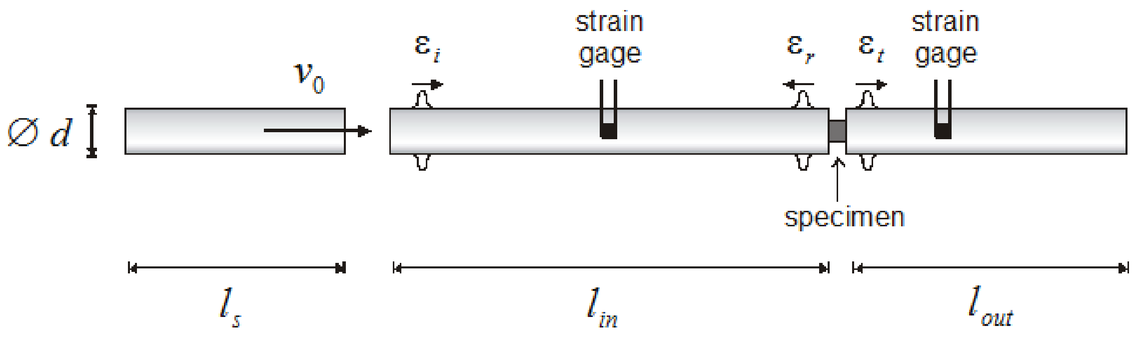

Figure 2-4: Schematic of a Split Hopkinson Pressure Bar system

2.4 Split Hopkinson Pressure bar systems

The experimental characterization of the mechanical behavior of a material at high rates of deformation requires specific experimental techniques. Issues particular to high strain rate testing include generating an appropriate loading pulse (a high velocity loading, of the order of 10m/s, with a rise time of a few tens of microseconds is required) and measuring forces applied to the tested specimens (in view of the extremely high accelerations occurring in high strain rate experiments, measured forces can easily be perturbed by spurious inertia effects). For an comprehensive review of high strain rate experimental techniques, the reader is referred to Field et al. (2004,[56])

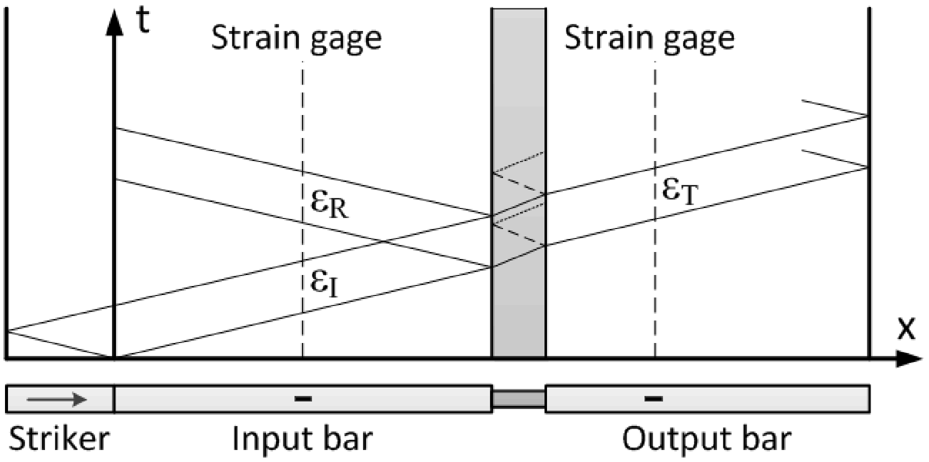

Figure 2-5: Wave-propagation diagram depicting the propagation of elastic waves in the SHPB system through space (horizontal axis) and time (vertical axis).

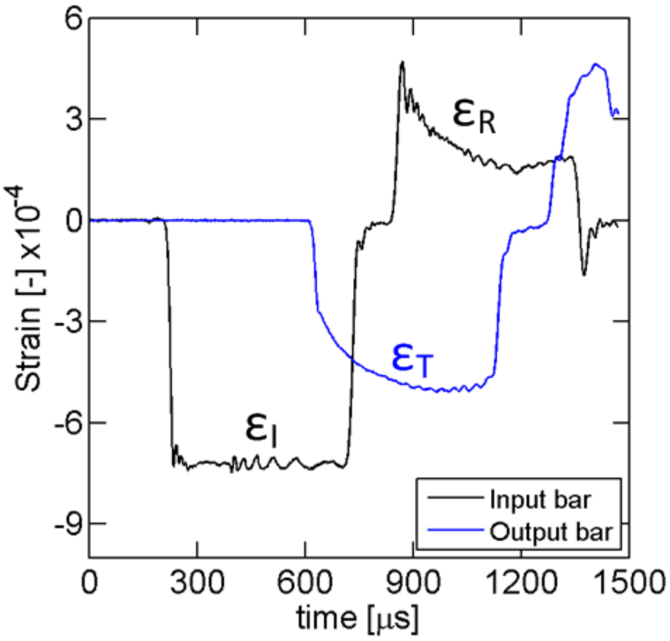

Figure 2-6: Example of signals measured in a SHPB experiment by the input (black line) and output (blue line) strain gages.

In this work, we will make use of a Split Hopkinson Pressure Bar (SHPB) system (Hopkinson, 1914, [80]; Davis, 1948, [43]; Kolsky, 1949, [96]) to perform high strain rate experiments. This type of apparatus has been widely used over the last 40 years to characterize the high strain rate behavior of materials under compression (e.g. Kolsky, 1949, [96]), and modified versions have been proposed for tension (e.g. Harding et al., 1960, [73]) or torsion (e.g. Duffy et al., 1971, [46]) loadings. SHPB systems permit to perform experiments with strain rates ranging from a few hundreds to a few thousands s^{-1}.

A typical SHPB system is shown in Fig. 2-4. It consists of two coaxial slender bars that sandwich the specimen to be tested. The bars can be made of steel, aluminum, polymers (e.g. Zhao et al., 1997, [200])… depending on the strength of the specimen. During an experiment, the free end of the input bar (left side in Fig. 2-4) is impacted by a slender striker at a velocity v_0. As a result, a compressive pulse is generated and propagates in the input bar towards the specimen. The propagation of the elastic waves in the system during an experiment is depicted in Fig. 2-5. When reaching the input bar/specimen interface, the loading pulse, or incident wave ε_I, is partially reflected in the input bar (reflected wave ε_R) and partially transmitted to the specimen. Similarly, when the wave inside the specimen reaches the specimen/output bar interface, it is partially reflected back in the specimen and partially transmitted to the output bar (transmitted wave ε_T). The time-history of the elastic waves are recorded at specific locations in the input and output bars by strain gages. Examples of measured signals are shown in Fig. 2-6. Strain waves at any locations within the bars, and especially at the bar/ specimen interfaces, are reconstructed using analytical methods that describe the propagation of longitudinal waves in elastic cylindrical bars (e.g. Zhao and Gary, 1995, [197]) and then used to obtain the forces and velocities applied by the bars to the specimen boundaries (see Section 3.3.2 for more details).